



Universiteit
Leiden
The Netherlands

The mass scale of high-redshift galaxies: virial mass estimates calibrated with stellar dynamical models from LEGA-C

Wel, A. van der; Houdt, J. van; Bezanson, R.; Franx, M.; D'Eugenio, F.; Straatman, C.; ... ; Holden, B.P.

Citation

Wel, A. van der, Houdt, J. van, Bezanson, R., Franx, M., D'Eugenio, F., Straatman, C., ... Holden, B. P. (2022). The mass scale of high-redshift galaxies: virial mass estimates calibrated with stellar dynamical models from LEGA-C. *The Astrophysical Journal*, 936(1).
doi:10.3847/1538-4357/ac83c5

Version: Publisher's Version
License: [Creative Commons CC BY 4.0 license](https://creativecommons.org/licenses/by/4.0/)
Downloaded from: <https://hdl.handle.net/1887/3561286>

Note: To cite this publication please use the final published version (if applicable).



The Mass Scale of High-redshift Galaxies: Virial Mass Estimates Calibrated with Stellar Dynamical Models from LEGA-C

Arjen van der Wel¹, Josha van Houdt², Rachel Bezanson³, Marijn Franx⁴, Francesco D'Eugenio⁵, Caroline Straatman⁵, Eric F. Bell⁶, Adam Muzzin⁷, David Sobral⁸, Michael V. Maseda⁴, Anna de Graaff⁴, and Bradford P. Holden⁹

¹ Sterrenkundig Observatorium, Universiteit Gent, Krijgslaan 281 S9, 9000 Gent, Belgium; arjen.vanderwel@ugent.be

² Max-Planck Institut für Astronomie Königstuhl, D-69117, Heidelberg, Germany

³ University of Pittsburgh, Department of Physics and Astronomy, 100 Allen Hall, 3941 O'Hara St, Pittsburgh PA 15260, USA

⁴ Leiden Observatory, Leiden University, P.O.Box 9513, NL-2300 AA Leiden, The Netherlands

⁵ Sterrenkundig Observatorium, Universiteit Gent, Krijgslaan 281 S9, 9000 Gent, Belgium

⁶ Department of Astronomy, University of Michigan, 1085 South University Ave., Ann Arbor, MI 48109, USA

⁷ Department of Physics and Astronomy, York University, 4700 Keele St., Toronto, Ontario, M3J 1P3, Canada

⁸ Department of Physics, Lancaster University, Lancaster LA1 4YB, UK

⁹ UCO/Lick Observatory, University of California, Santa Cruz, CA 95064, USA

Received 2022 March 21; revised 2022 June 2; accepted 2022 June 14; published 2022 August 25

Abstract

Dynamical models for 673 galaxies at $z = 0.6\text{--}1.0$ with spatially resolved (long-slit) stellar kinematic data from LEGA-C are used to calibrate virial mass estimates defined as $M_{\text{vir}} = K\sigma_{*,\text{int}}^2 R$, with K a scaling factor, $\sigma'_{*,\text{int}}$ the spatially integrated stellar velocity second moment from the LEGA-C survey, and R the effective radius measured from a Sérsic profile fit to Hubble Space Telescope imaging. The sample is representative for $M_* > 3 \times 10^{10} M_{\odot}$ and includes all types of galaxies, irrespective of morphology and color. We demonstrate that using $R = R_{\text{sma}}$ (the semimajor axis length of the ellipse that encloses 50% of the light) in combination with an inclination correction on $\sigma'_{*,\text{int}}$ produces an unbiased M_{vir} . We confirm the importance of projection effects on $\sigma'_{*,\text{int}}$ by showing the existence of a similar residual trend between virial mass estimates and inclination for the nearby early-type galaxies in the ATLAS^{3D} survey. Also, as previously shown, when using a Sérsic profile-based R estimate, a Sérsic index-dependent correction to account for nonhomology in the radial profiles is required. With respect to analogous dynamical models for low-redshift galaxies from the ATLAS^{3D} survey we find a systematic offset of 0.1 dex in the calibrated virial constant for LEGA-C, which may be due to physical differences between the galaxy samples or an unknown systematic error. Either way, with our work we establish a common mass scale for galaxies across 8 Gyr of cosmic time with a systematic uncertainty of at most 0.1 dex.

Unified Astronomy Thesaurus concepts: [Galaxy evolution \(594\)](#); [Galaxy dynamics \(591\)](#); [Scaling relations \(2031\)](#); [Galaxy masses \(607\)](#)

Supporting material: machine-readable table

1. Introduction

The total mass of a galaxy is perhaps the single most important of its properties. At all cosmic times, it is related to a host of other properties, such as the stellar mass (e.g., Taylor et al. 2010), star formation rate (Brinchmann et al. 2004; Noeske et al. 2007), size (e.g., Shen et al. 2003; van der Wel et al. 2014a), average stellar age (e.g., Gallazzi et al. 2005, 2014; Wu et al. 2018), and rotational properties (e.g., Emsellem et al. 2007). Furthermore, a galaxy can be plausibly linked to its progenitors through its mass, which changes through time due to passive growth or mergers (e.g., Bezanson et al. 2009; Naab et al. 2009). Deriving accurate, unbiased masses is therefore an obvious priority in any galaxy survey.

For spatially integrated kinematic measurements we define the virial mass using the scalar virial theorem:

$$M_{\text{vir}} = K \frac{\sigma^2 R}{G}, \quad (1)$$

with G the gravitational constant, R the radius of the galaxy, σ the velocity second moment, strictly speaking, only equal to the velocity dispersion for a nonrotating galaxy, and K a scaling factor. All of these quantities, with the exception of G , are at this point only generically defined and their exact definition is, in essence, the topic of this paper.

The parameters used in this M_{vir} estimate only crudely approximate the kinematic and geometric structure of galaxies and are therefore susceptible to both random and systematic uncertainties. Two approaches have been used to address this issue: comparison with dynamical models, and comparison with stellar mass estimates from photometry. First, dynamical models provide an accurate absolute mass scale with which M_{vir} estimates can be compared. Such an empirical calibration was done for the SAURON survey in Cappellari et al. (2006) and revisited by the ATLAS^{3D} collaboration in Cappellari et al. (2013, hereafter C06 and C13, respectively). This volume-limited sample of morphologically selected early-type galaxies produces a large dynamic range in mass, but the number of high-mass galaxies is relatively small. Larger surveys across all galaxy types (Sánchez et al. 2012; Bundy et al. 2015; Scott et al. 2018) have not revisited this calibration, even though this would be relatively straightforward with the dynamical models for 2000 galaxies in MANGA at $z \lesssim 0.1$ published by Li et al. (2018).

Second, a comparison between M_{vir} and stellar mass estimates M_* provides an idea of the precision of both parameters (Taylor et al. 2010). The average value and scatter in M_*/M_{vir} are informative, but both quantities suffer from systematics, again leaving the absolute mass scale uncertain. This method is popular at higher redshifts (van der Wel et al. 2006; van de Sande et al. 2013; Belli et al. 2014) where (until now) dynamical models have been difficult to construct, resulting in small and biased samples of old, massive galaxies (van Dokkum & van der Marel 2007; van der Wel & van der Marel 2008; Shetty & Cappellari 2015; Guérou et al. 2017; Newman et al. 2018).

In this paper we make progress in addressing these issues by using nearly 800 galaxies in the $z = 0.6\text{--}1$ redshift range from the LEGA-C survey (van der Wel et al. 2016, 2021) with dynamical models from (van Houdt et al. 2021, hereafter vH21). This sample includes all types of galaxies as the selection was blind to structure and color. Using mass estimates from the dynamical models we will establish the normalization K , show that the use of a circularized radius should be avoided, and introduce a necessary but simple inclination correction for the integrated velocity second moment. We assume a Λ CDM cosmology with $H_0 = 70 \text{ km s}^{-1}$, $\Omega_\Lambda = 0.7$, and $\Omega_M = 0.3$.

2. Data and Methods

This work is based on the Large Early Galaxy Astrophysics Census survey (LEGA-C; the survey description and further details can be found in van der Wel et al. 2016; Straatman et al. 2018; van der Wel et al. 2021). This survey provides exceptionally deep, spatially resolved spectra for approximately 4000 mag limited galaxies from the UltraVISTA photometric parent catalog (Muzzin et al. 2013a), targeted at redshifts between 0.6 and 1.0. Spectra have been obtained with the VIMOS instrument on the Very Large Telescope. With ~ 20 hr of integration per object, $R \sim 3500$ spectra are produced with a wavelength coverage between ~ 6300 and $\sim 8800 \text{ \AA}$.

In this paper, we use the subset of galaxies drawn from the third data release (DR3; van der Wel et al. 2021) suitable for kinematic modeling described in full by van Houdt et al. (2021). Galaxies are selected to have high signal-to-noise ratio ($> 10 \text{ \AA}^{-1}$), measured $\sigma'_{*,\text{int}}$ (see below for the definition), have major axes aligned within 45° of the direction of the slit, and have imaging data show a regular morphology that is well described by a Sérsic profile (FLAG_MORPH = 0 in DR3).

Stellar and gas kinematics are derived from the spectra using pPXF¹⁰ (Cappellari & Emsellem 2004; Cappellari 2017). In summary, a combination of single stellar population templates and Gaussian emission lines are fit to the observed spectra. The theoretical spectra are broadened and shifted to find the spatially resolved rotation and dispersion, independently for the gas and stars. This is done for 2D and 1D spectra, where the former is used for the Jeans models (see below) and the latter is used to extract the integrated velocity second moment $\sigma'_{*,\text{int}}$, which are used to calculate the virial masses. For further details on the spectral modeling, see Bezanson et al. (2018b, 2018a). The notation $\sigma'_{*,\text{int}}$, introduced by Bezanson et al. (2018a), is chosen to differentiate between the spatially integrated velocity broadening along the line of sight and the intrinsic velocity dispersion σ_* .

Optical imaging is available for each galaxy with HST/Advanced Camera for Surveys (ACS) F814W observations

(Koekemoer et al. 2007). Structural parameters are extracted with single-component Sérsic fits using GALFIT¹¹ (Peng et al. 2010) as described in van der Wel et al. (2012) and DR3. All three main parameters from the Sérsic fit—Sérsic index, effective radius, and projected axis ratio—play a key role in this work and their use in Equation (1) is, essentially, the topic of this paper.

The dynamical masses to which the virial masses will be scaled were obtained from Jeans models as presented by van Houdt et al. (2021). Summarizing, the galaxies are modeled as oblate axisymmetric spheroids as implemented in the Jeans anisotropic multi-Gaussian expansion (JAM) code (Cappellari 2008).¹² The surface brightness is parameterized by the Sérsic profiles derived from the HST/ACS F814W imaging, decomposed into a series of Gaussians using the multi-Gaussian expansion (MGE;¹³ Cappellari 2002) code. The probability density of the inclination is assumed to be a function of the observed axis ratio, using observationally derived intrinsic shape distributions (Chang et al. 2013; van der Wel et al. 2014b; van Houdt et al. 2021). The slit geometry of the LEGA-C spectroscopy is included in the models: the Jeans equations are integrated through rectangular $1'' \times 0''.205$ apertures, instrumental velocity gradients are subtracted, and the centering of the slit is marginalized over in the Bayesian fitting approach. The model predictions of v_{rms} are compared with the measured $\sqrt{v'^2_* + \sigma'^2_*}$, where v'_* and σ'_* are the measured line-of-sight velocity first and second moments for each spatial element, typically reached $1''\text{--}1''.5$ or $1\text{--}3$ effective radii along the slit direction.

There are two components in the gravitational potential: the stellar component (for which we assume that mass follows light as seen in the HST image) and a dark matter component, parameterized by a Navarro–Frenk–White halo. We do not claim to constrain the dark matter mass directly, but the inclusion of a dark component is required by the data and allows greater flexibility in fitting a gradient in the mass-to-light ratio regardless of its origin (stellar M/L , stellar initial mass function, gas, dark matter), and therefore produces more realistic uncertainties.

In vH21 we already published mass estimates and proxies for dynamical structure (e.g., V/σ), but to facilitate comparisons with other data sets and models we present in the Appendix the fitted parameters and model components. In this paper we use the sample of 673 galaxies selected to have JAM mass estimates within R_e with a precision better than 0.5 dex. This is 22% of the sample of galaxies for which we can estimate virial masses based on the integrated $\sigma'_{*,\text{int}}$, which is essentially the full LEGA-C primary, K -band selected sample described by van der Wel et al. (2021). As explained by vH21, many galaxies do not have a Jeans mass estimate because their major axis is misaligned with the LEGA-C slit by more than 45° ($\sim 50\%$, given the random position angle distribution), while other galaxies do not have spectra with sufficient signal-to-noise. However, as we will discuss further below, we find no correlations between the virial-to-Jeans mass ratio and any other parameter, which implies that our derived virial mass estimates can be applied generally to galaxies in the mass and redshift range of LEGA-C, which samples galaxies with stellar masses $\gtrsim 2 \times 10^{10} M_\odot$ and $50 \lesssim \sigma'_*/(\text{km s}^{-1}) \lesssim 300$, at $0.6 < z < 1$.

¹¹ v3.0.5, available at <https://users.obs.carnegiescience.edu/peng/work/galfit/galfit.html>.

¹² v5.0.17 from <https://pypi.org/project/jampy/>.

¹³ v5.0.12, from <https://pypi.org/project/mgefit/>.

¹⁰ v6.0.0, via <http://www-astro.physics.ox.ac.uk/~mxc/software/>.

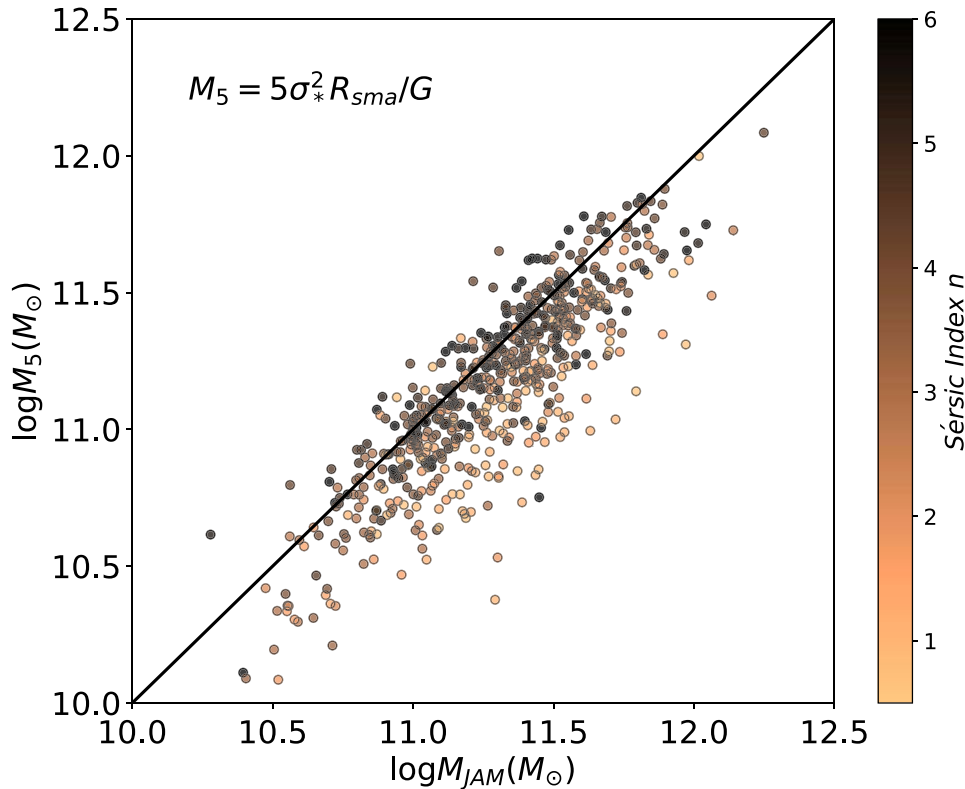


Figure 1. The simplest virial mass estimator, M_5 , vs. M_{JAM} , color-coded with Sérsic index n . For low- n galaxies M_{JAM} is systematically larger than M_5 , implying that a nonhomology correction is required to properly scale the virial mass estimator.

3. Calibration of the Virial Mass

Conceptually, there are two critical aspects that need to be addressed when estimating virial masses based on integrated velocity dispersions (or, to be more precise, second moments) and effective radius measurements: how nonhomology in radial structure affects the virial mass (discussed in Section 3.1) and how to take into account nonhomology in the 3D geometry of galaxies and the resulting projection effects on the observables (discussed below in Section 3.2).

3.1. Nonhomology in Radial Structure

We define the total dynamical mass from the best-fitting Jeans models as $2 \times$ the Jeans model mass enclosed within a sphere with radius R_{sma} , the semimajor axis of the ellipse that contains 50% of the (projected) Sérsic light model:

$$M_{\text{JAM}} \equiv 2 \times M(r < R_{\text{sma}}). \quad (2)$$

This ensures that both mass estimates are approximately based on the same luminosity; essentially, our comparison is between mass-to-light ratios. The choice for R_{sma} is motivated in Section 4.1, which also includes a broader discussion on the concept of using any galactic radius as a proxy for virial radius.

As a starting point we calculate a simple virial mass estimate that is only proportional to R_{sma} and $\sigma_{*,\text{int}}^2$, the observed (projected) velocity second moment:

$$M_5 = 5 \frac{\sigma_{*,\text{int}}^2 R_{\text{sma}}}{G}. \quad (3)$$

The constant scaling factor 5 has been often used as a practical tool without explicit justification (e.g., Bender et al. 1992;

Jorgensen et al. 1996; van der Wel et al. 2006; Toft et al. 2012). To place this normalization on a firmer basis, C06 provided a calibration using detailed dynamical models as we do here. They found that, when the effective radius is measured in a then “classic” way using an $r^{1/4}$ growth-curve extrapolation (Dressler et al. 1987; Jorgensen et al. 1996), the best-fitting coefficient was indeed $K = 5.0 \pm 0.1$.

In Figure 1 we compare M_5 with M_{JAM} . There is a strong trend with Sérsic index n ; clearly, galaxies are not self-similar in detail. In Figure 2 we explicitly show this n dependence in comparison with the proportionality factor,

$$K(n) = 8.87 - 0.831n + 0.0241n^2. \quad (4)$$

$K(n)$ is the scaling factor taken from C06 (Equation (20)). The residual correlation between M_5 with M_{JAM} follows this description very well, indicating that this nonhomology correction is required. This agrees with the finding by Taylor et al. (2010), who compared stellar masses from population with virial mass estimates. It also agrees with the results by C13, who used JAM dynamical models as we do here and also concluded that the above nonhomology correction is needed when the effective radius is measured from Sérsic models as we do here. However, we are now left with a strong residual correlation with the projected axis ratio: round galaxies have larger $M_{\text{JAM}}/M_{\text{vir}}$ than flat galaxies, signaling the importance of nonhomology in 3D galaxy structure (in essence, spheres and disks) and the resulting projection effects on both the kinematics and the light distribution.

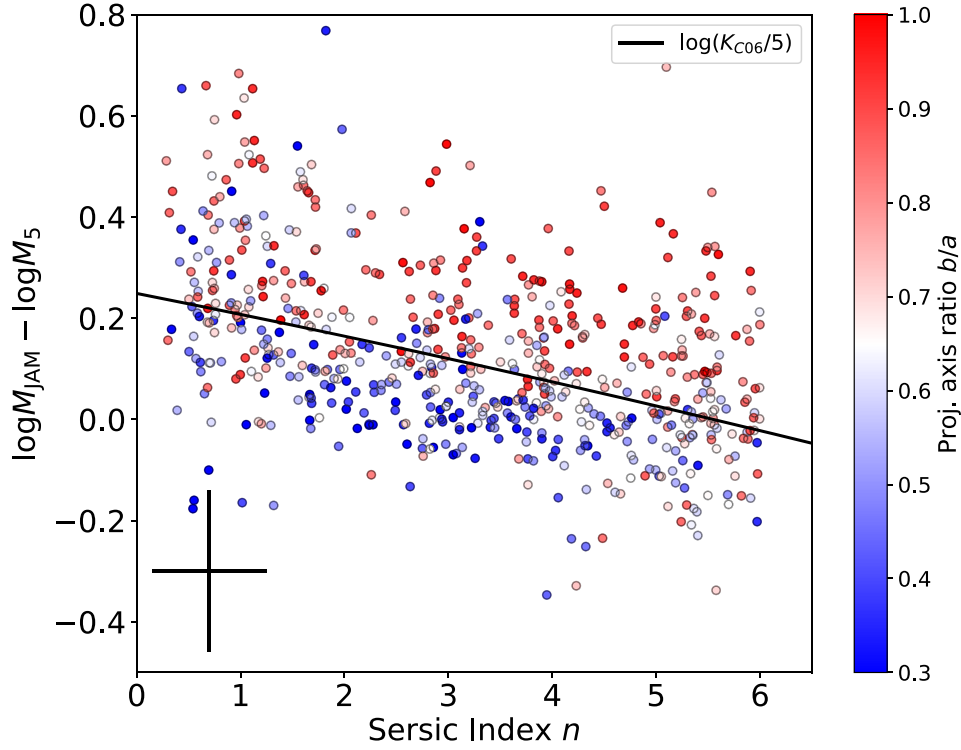


Figure 2. Ratio of M_{JAM} and M_5 (see Figure 1) vs. Sérsic index n , color-coded with the projected axis ratio b/a . The black line represents the proportionality factor $K(n) = 8.87 - 0.831n + 0.0241n^2$ from Cappellari et al. (2006) divided by a factor 5 (from M_5), which describes the n dependence well. But a strong residual correlation with the projected axis ratio is readily apparent, implying that a viewing angle correction is required to properly scale the virial mass estimator.

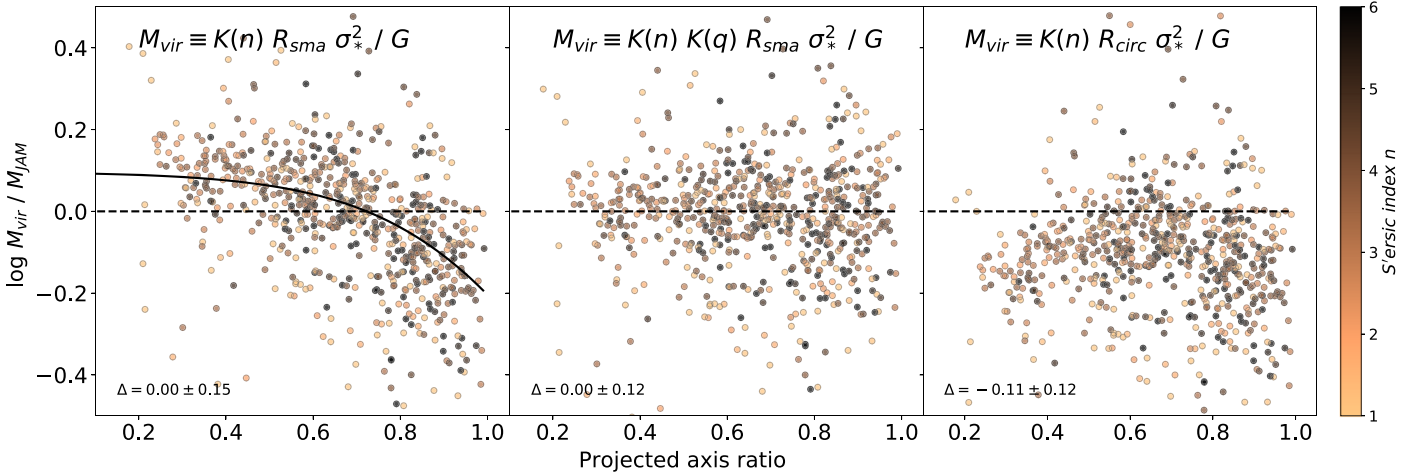


Figure 3. The ratio between homology-corrected virial mass and Jeans mass for three different definitions of the virial mass (as indicated in the panels) vs. the projected axis ratio. Left: M_{vir} with R_{sma} and $\sigma_{*,\text{int}}$. The black line in the left-hand panel is a fit to the axis ratio trend and functions as the structural homology correction $K(q)$ (Equation (6)). This correction is applied to M_{vir} in the middle panel. Right: M_{vir} with R_{circ} instead of R_{sma} and without $K(q)$.

3.2. Nonhomology in 3D Galaxy Structure and Projection Effects

The projected axis ratio q reflects the combination of the intrinsic, 3D geometry of a galaxy and the viewing angle. We use the residual trend with q in Figure 2 to derive a second structural homology correction to account for variations in galaxy geometry that also includes projection effects. We do so purely empirically, by removing the residual trend with the axis ratio q .

In the left-hand panel of Figure 3 we show the same residual trend with q as in Figure 2 but now explicitly as a function of

q and adopting the virial mass

$$M_n = K(n) \frac{\sigma_{*,\text{int}}^2 R_{\text{sma}}}{G} \quad (5)$$

that includes the radial nonhomology correction $K(n)$. With this definition, galaxies that are round in projection have underestimated virial masses; that is, the projected velocity second moment of nearly face-on, rotating galaxies do not “see” galactic rotation. It is important to note here that the velocity dispersion used in the virial mass estimate must include all sources of motion in the galactic potential: not only the

quasi-random motions associated with the true velocity dispersion at a given location in a galaxy, but also organized motions such as rotation. But a striking feature is that there is no systematic offset between M_n and M_{JAM} . Apparently, variations in geometry and projection effects do not cause a systematic difference between simple virial mass estimates and more accurate dynamical models using spatially resolved kinematics.

We now introduce the homology correction $K(q)$:

$$K(q) = (0.87 + 0.38e^{-3.78(1-q)})^2, \quad (6)$$

which is the inverse of the solid line in the left-hand panel of Figure 3. This analytical form is purely practical and has no physical basis. For a given geometry and dynamical structure, an inclination correction can be derived from the dynamical model or calculated directly from the tensor virial theorem (Bender et al. 1992), but our sample consists of a set of galaxies with a large variety in structure.

The middle panel of Figure 3 shows the distribution of $M_{\text{vir}}/M_{\text{JAM}}$ according to our best-effort virial mass estimate:

$$M_{n,q} = K(n)K(q) \frac{\sigma_{*,\text{int}}'^2 R_{\text{sma}}}{G}, \quad (7)$$

which is now independent of q (by construction) and for which the variance is reduced by $\sim 1/3$ (the new rms is 0.12 dex).¹⁴ Importantly, no dependence on Sérsic index is reintroduced: on average, the inclination correction works well for both high- and low- n galaxies.

As mentioned before, the norm in the literature on virial mass estimates of high-redshift galaxies has been to choose the circularized radius $R_{\text{circ}} \equiv \sqrt{q} R_{\text{sma}}$. This is motivated by the result that the stellar-to-virial mass ratio produces smaller scatter when R_{circ} is in a virial mass estimate, both at low redshift (Cappellari et al. 2013) and at high redshift (Belli et al. 2017), where the latter interpret this as evidence for rotational support via tentative residual correlations with the axis ratio and Sérsic index.

In the right-hand panel of Figure 3 we show the result of using R_{circ} (and $K(n)$ but not $K(q)$). Compared to the left-hand panel there is a much weaker trend with the axis ratio. The factor \sqrt{q} —replacing our $K(q)$ —acts as a reasonably good homology correction, but this comes at the expense of a systematic offset. This offset is to be expected since the virial mass is now derived on the basis of a smaller radius than the Jeans model mass (by approximately a factor \sqrt{q}), but reducing the Jeans model mass by recalculating it within a sphere of radius R_{circ} instead of R_{sma} would reintroduce the same axis ratio trend as seen in the left-hand panel.

4. Discussion

4.1. The Choice of Virial Radius

Defining the virial radius of a galaxy is conceptually problematic. The only true virial radius is that of the dark matter halo, but this is not traced by the luminous body. In this paper, implicitly making several assumptions and approximations, we equate the virial radius with R_{sma} , the semimajor axis

of the ellipse that contains 50% of the light in the HST ACS/F814W image, and we compare the inferred virial mass estimate with the Jeans model mass calculated within a *sphere* with the same radius. Specifically, we assume that (1) the sphere with radius R_{sma} contains 50% of the 3D luminosity distribution; and (2) R_{sma} measured at a rest-frame wavelength of $\sim 4000\text{--}5000 \text{ \AA}$ by fitting a 2D Sérsic profile can be used as proxy for the spatial extent of galaxies.

The first of these assumptions was first addressed by Ciotti (1991), who showed that for a spherical galaxy with a Sérsic profile $r_{1/2}/R_{\text{sma}} = 1.34\text{--}1.36$ for Sérsic indices $n = 2\text{--}10$ (here, $r_{1/2}$ is the radius of a sphere that contains 50% of the 3D light distribution). But for disk galaxies this value decreases and approaches unity (C13). A key consideration is, then, that most galaxies ($\sim 90\%$) in the LEGA-C sample analyzed in this paper are rotating, rather flat (intrinsic $c/a \approx 0.3$) and nearly axisymmetric systems as evidenced by both their projected shape distribution (Chang et al. 2013; van der Wel et al. 2014b) and their kinematics (vH21). This large fraction of highly flattened galaxies is not specific to the LEGA-C sample: galaxies in the present-day universe, including massive quiescent/early-type galaxies, generally have similar shapes (e.g., Chang et al. 2013) and commonly show a large degree of rotational support (e.g., Emsellem et al. 2011). van de Ven & van der Wel (2021) show that for such flattened, oblate galaxies the difference between the projected R_{sma} and $r_{1/2}$ of a sphere is negligible. A minor caveat is that for slowly rotating triaxial galaxies (and more generally, galaxies with nondisklike geometries, in total about 10% of the LEGA-C sample) R_{sma} and $r_{1/2}$ can differ: van de Ven & van der Wel (2021) find that for massive, triaxial ellipticals $r_{1/2}/R_{\text{sma}} = 1.18 \pm 0.18$, where the error reflects the galaxy-to-galaxy scatter due to variations in intrinsic shape and viewing angle.

These considerations generalize the conclusions from previous work by Hopkins et al. (2010) and Cappellari et al. (2013) who showed that R_{sma} is largely independent of inclination and is therefore the preferred size proxy (rather than R_{circ}). We return to this issue in Section 5.2 when we examine the mass offset we see in Figure 3 when using circularized radii (right-hand panel) and comparing with M/L measurements from the ATLAS^{3D} survey of nearby early-type galaxies.

The second crucial assumption made explicit above (that the rest-frame $\sim 4000\text{--}5000 \text{ \AA}$ R_{sma} from a Sérsic fit is a good proxy for galaxy size) is more difficult to defend. The observed color gradients (e.g., van der Wel et al. 2012) imply that R_{sma} is wavelength dependent (also see Kelvin et al. 2012), which in turn implies the presence of mass-to-light gradients (Szomoru et al. 2013; Mosleh et al. 2017; Suess et al. 2019). If the inner parts of galaxies are dominated by stars, then the more sensible choice of the virial radius might be a mass-weighted half-light radius. At the same time, gas and dark matter fractions increase with radius, creating M/L gradients in the opposite direction. Color gradient information is currently not available for the full sample of galaxies studied here. We should therefore keep in mind that our definition of the galaxy mass scale is set by our choice of R_{sma} as the optical half-light radius, measured at $\sim 4000\text{--}5000 \text{ \AA}$, a choice that is to some extent arbitrary as it is determined by the available data.

In addition, our R_{sma} (and the stellar profile used in the Jeans dynamical model) relies on the Sérsic profile. A comparison between Sérsic model magnitudes and large-aperture ground-based photometric magnitudes convinces us that the Sérsic

¹⁴ LEGA-C DR3 includes two quantities related to the stellar velocity dispersion: the measured stellar velocity second moment $\text{SIGMA_STAR-S_PRIME}$ (written as $\sigma_{*,\text{int}}$ in this paper) and $\text{SIGMA_STARS_VIR} = \sqrt{K(q)} \times \text{SIGMA_STARS_PRIME}$.

profile is appropriate: the difference (accounting for differences in filter transmission curves) is, on average, just 0.02 mag, with 0.15 mag scatter. In particular, the Sérsic model does not unduly extrapolate the light profile, artificially increasing the luminosity and the radius. We therefore believe the total luminosities to be accurate. This, in turn, implies that both $M_{\text{JAM}}(R < R_{\text{sma}})$ and $M_{\text{vir}}/2$ —the approximate mass estimates within radius R_{sma} —are accurate in relation to each other. The multiplication by a factor 2 is an unverified extrapolation and only serves to account for the total luminosity and to enable comparisons with, e.g., total stellar mass inferred from spatially integrated photometry.

Finally, for some purposes the circularized radius R_{circ} can be more useful. Traditionally, fundamental plane studies use R_{circ} and the projected axis ratio q does not factor in. When q is not available (for example, when sizes are derived from growth curves and circular apertures), then our $K(q)$ correction does not apply. Also, for extremely elongated, prolate galaxies R_{circ} is the more stable size proxy (compared to $r_{1/2}$). But overall, given the weak viewing angle dependence of $R_{\text{sma}}/r_{1/2}$ for most galaxy geometries encountered in nature, we recommend the use of R_{sma} and the virial mass estimate from Equation (7).

4.2. Residual Correlations

As discussed in Section 3, correlations in $M_{\text{vir}}/M_{\text{JAM}}$ with Sérsic n and projected shape have been accounted for and removed in our final M_{vir} estimate. We find no significant correlations with any other parameter that is available for our sample. In particular, there is no difference between large and small galaxies, high- and low-mass galaxies, and no dependence on star formation activity (Figure 4). Furthermore, we do not find a trend with redshift.

Most importantly, in Figure 5 we show that there is no residual correlation with the rotation parameter κ derived from the Jeans models (see van Houdt et al. 2021, for details). This is in contrast with the findings of van der Wel & van der Marel (2008), who find that fast-rotating galaxies overestimate the virial mass by as much as 0.2 dex. However, that comparison is done at fixed $K = 5$. As we show here, and demonstrated earlier for present-day galaxies (C13), a nonhomologous scale factor should be used to derive unbiased masses, at least when using a Sérsic profile-based effective radius. Using $K(n) = 5$, we find a difference of at most 0.1 dex between the fast-rotating galaxies ($\kappa > 0.5$) and slow-rotating galaxies ($\kappa < 0.5$). Whether or not this entirely explains the results from van der Wel & van der Marel (2008) remains unclear, but this discrepancy is indicative of the importance of using consistent measurements when deciding which normalization to use and when comparing galaxies across different epochs.

The newly calibrated virial mass estimates also apply equally, in a systematic sense to within 10% or 0.04 dex, to quiescent and star-forming galaxies (Figure 4). The sample is separated based on their rest-frame $U - V$ and $V - J$ colors. Both types show no systematic difference between M_{vir} and M_{JAM} , but star-forming galaxies show larger scatter. The scatter is consistent with the formal uncertainties in the M_{JAM} estimates. These are slightly larger than the formal uncertainties on M_{vir} due to the added flexibility provided by the dark matter component in the JAM model. The uncertainties for the star-forming galaxies are larger than for the quiescent galaxies for several reasons: (1) the $\sigma'_{*,\text{int}}$ measurements are less precise as a result of a lower signal-to-noise ratio; (2) the stellar light

profiles likely suffer from stronger deviations from the mass-follows-light assumption for the stellar component due to dust and star-forming regions; and (3) gas and dark matter fractions are likely higher.

5. Comparison with ATLAS^{3D}

The JAM-based mass models from the ATLAS^{3D} survey (Cappellari et al. 2013, C13) have served as the standard benchmark for virial mass estimates. The motivation for our work is to directly determine the normalization of the virial mass for galaxies at large lookback time, reducing potential observational biases and evolutionary effects. The self-consistent, mass-follows-light dynamical models for the ATLAS^{3D} data from C13 take MGE models as the light and mass tracer; Sérsic profiles are fitted independently by Krajnović et al. (2013) but are not used in the modeling. C13 provide two separate virial mass estimates for the MGE light model (here, referred to as $M_{\text{vir},l}$) and the Sérsic light model (here, referred to as $M_{\text{vir},n}$). In Section 5.1 we examine the residual trend with projected axis ratio in the M_{vir} estimates for the ATLAS^{3D} sample, and in Section 5.2 we discuss a systematic difference of 0.1 dex between LEGA-C and ATLAS^{3D} mass estimates.

5.1. A Dependence of the Virial Mass on Projected Axis Ratio in ATLAS^{3D}

The left-hand panel of Figure 6 compares $(M/L)_{\text{JAM}}$ and $(M/L)_{\text{vir}}$ where both are based on the MGE light model, and where M_{vir} is defined in C13. This reveals a significant and hitherto hidden dependence on projected axis ratio, analogous to the trend seen for LEGA-C in this paper. With this new insight we define a new virial mass estimate for ATLAS^{3D} (shown in the right-hand panel of Figure 6):

$$M_{\text{vir,A3D}} = 3.6 \frac{\langle V_{\text{rms},e}^2 \rangle R_{\text{MGE,maj}}}{G}, \quad (8)$$

where $\langle V_{\text{rms},e}^2 \rangle$ is the deprojected second moment of the velocity, from Equation (29) of C13.¹⁵ This is the quadratic sum of the velocity dispersion σ and the inclination-corrected velocity $V/\sin i$, averaging (light-weighted) over all spatial elements within the MGE half-light ellipse. Here, i is the inclination inferred from the JAM. This inclination-corrected $\langle V_{\text{rms},e}^2 \rangle$ is not an empirical function of the observed axis ratio (as in Equation (6) of this paper), but derives from the projected shape of the kinematics and the inclination, simultaneously removing the trend with the axis ratio and reducing the scatter in the virial mass estimate. Specifically, the scatter in the ratio decreases from 0.08 dex in the left-hand panel to 0.06 dex in the right-hand panel. This result confirms one of the main findings of this paper for ATLAS^{3D}: the scatter in the virial estimates and the dependency on q is partially due to the effect of inclination on the measured second velocity moment. The normalization factor is reduced from 3.9 to 3.6 in order to remove an offset with respect to $(M/L)_{\text{JAM}}$ (since generally $\langle V_{\text{rms},e}^2 \rangle > \sigma_{\text{Re}}^2$). Note that no Sérsic index dependence enters in the above: the mixed use of MGE light models for JAM and a Sérsic index-based homology correction is generally not recommended (also see C13).

¹⁵ The values are available from <https://purl.org/atlas3d>.

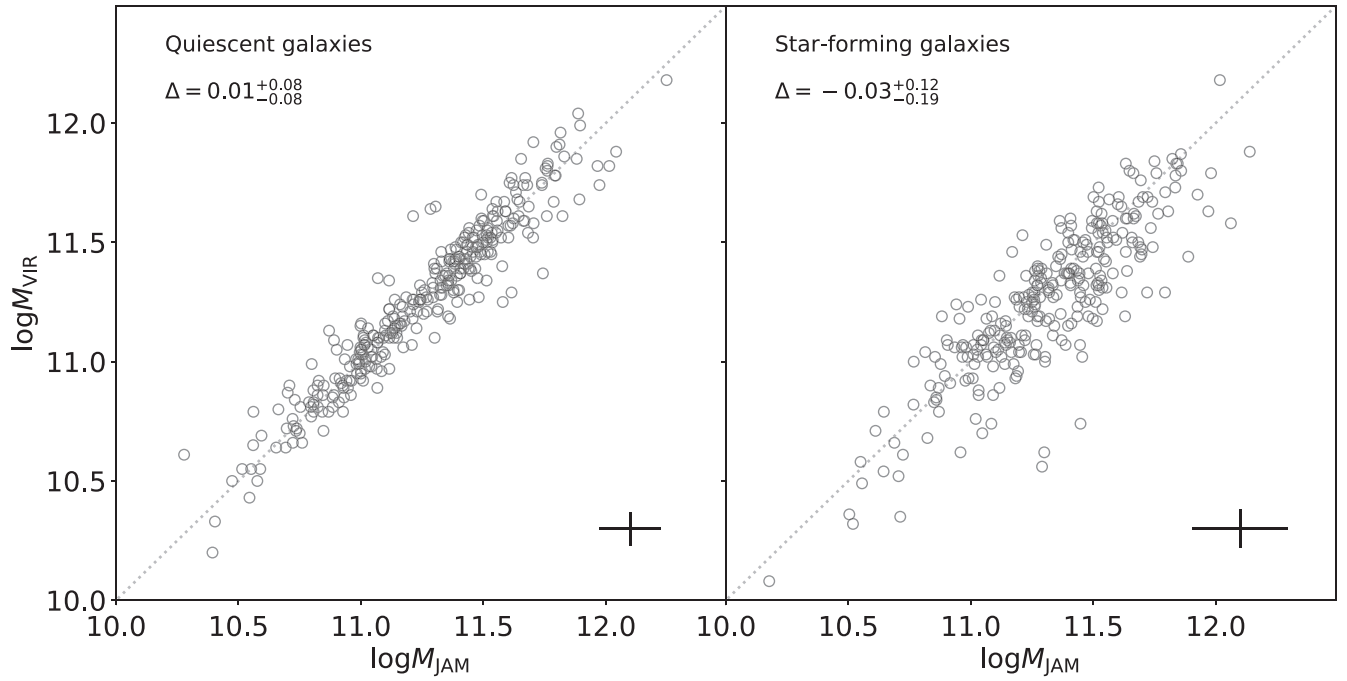


Figure 4. Virial mass vs. JAM mass, separately for quiescent and star-forming galaxies. Our newly constructed virial mass agrees very well with the JAM mass, without systematic bias. The random uncertainty (as indicated by the scatter) is larger for star-forming galaxies than for quiescent galaxies.

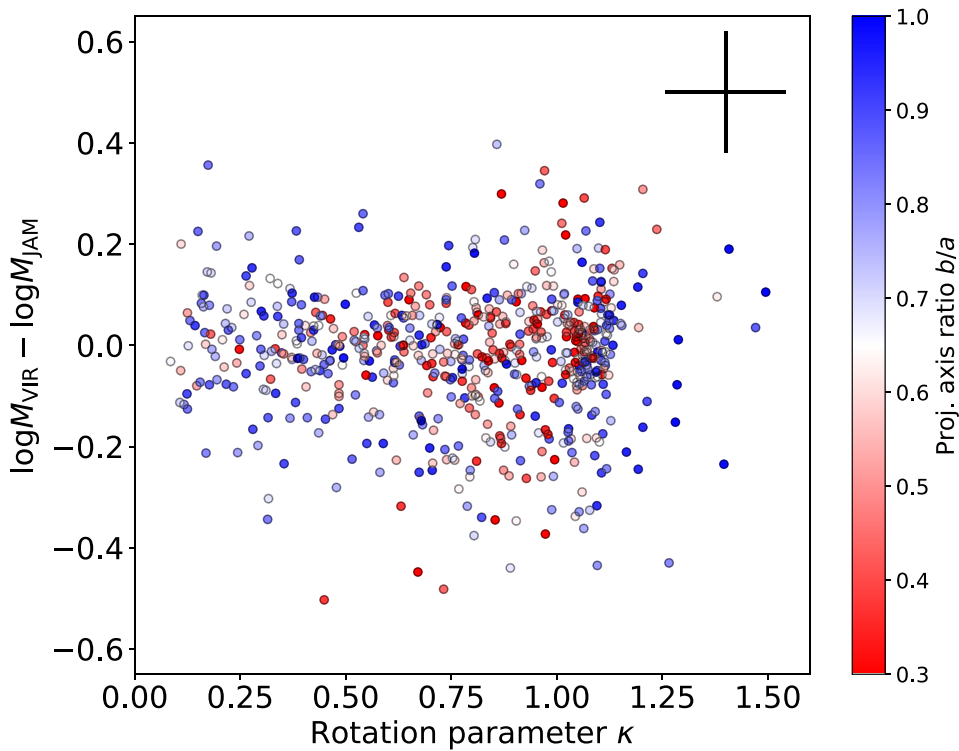


Figure 5. $M_{\text{vir}}/M_{\text{JAM}}$ vs. rotation parameter κ calculated from the Jeans dynamical model, color-coded with projected axis ratio. κ ranges from ~ 0 for nonrotating galaxies to ~ 1 for galaxies that are rotationally supported. Note that the dynamical model distinguishes between galaxies that are round in projection (color-coded with blue) that are face-on disks and galaxies that are intrinsically round and nonrotating. There is no bias in our M_{vir} estimates that depends on the orbital structure of the galaxy; our inclination correction $K(q)$ serves to account for any such dependence.

5.2. A Systematic Offset between LEGA-C and ATLAS^{3D}

C13 also provide a Sérsic-based $M_{\text{vir,n}}$ estimate, which uses $K(n)$ (here, Equation (4)) and R_{circ} . We already saw in Section 3.2 and Figure 3 (right-hand panel) that this definition

produces a mass offset with respect to the LEGA-C JAM estimates, suggesting a systematic difference between the LEGA-C and ATLAS^{3D} mass scales, which we examine here.

As a first step we show for ATLAS^{3D} that $(M/L)_{\text{vir,n}}$ is independent of the axis ratio (left-hand panel of Figure 7),

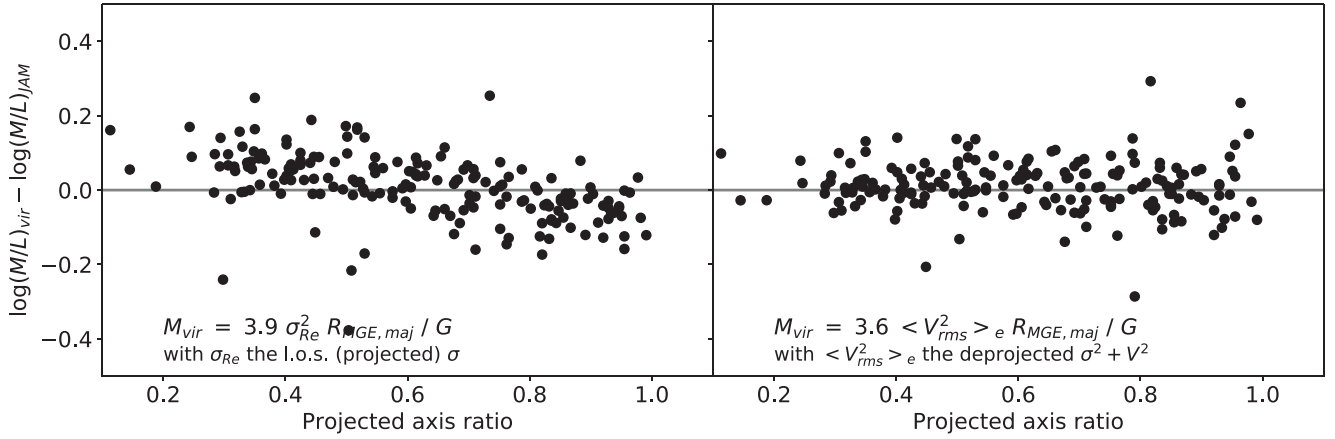


Figure 6. Comparison of MGE-based virial M/L with JAM M/L for ATLAS^{3D} from C13 as a function of the projected axis ratio. Galaxies with quality flag 0 (see C13) are removed from the sample. Left: M_{vir}/L as defined by C13 for MGE parameters; Right: a revised M_{vir}/L for MGE parameters using the inclination correction velocity estimator $\langle V_{\text{rms}}^2 \rangle_e$ from C13. See the text for details.

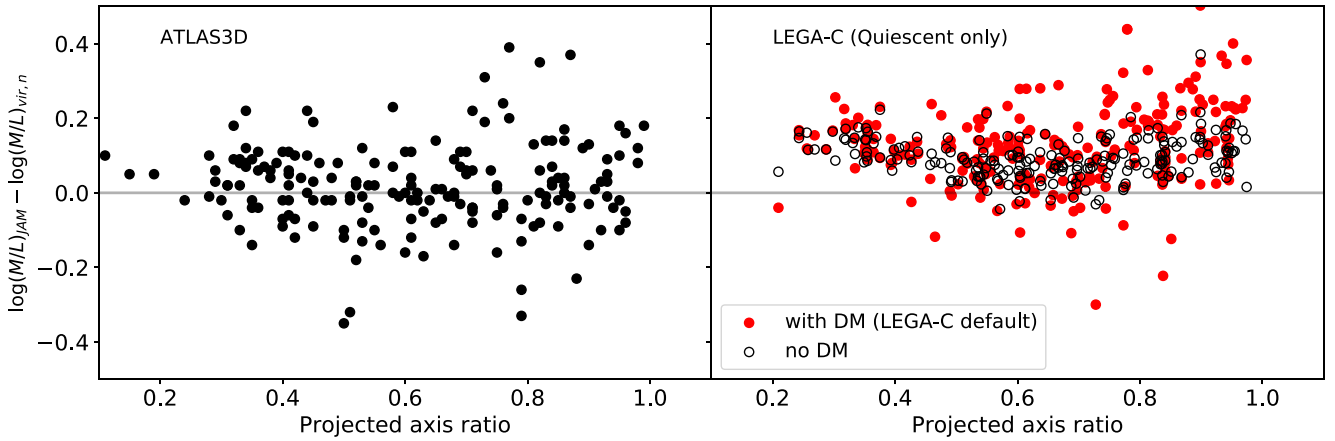


Figure 7. Comparison of JAM (M/L) from ATLAS^{3D} (left) and LEGA-C (right) with the Sérsic profile-based virial M/L estimates as defined for ATLAS^{3D} by C13 ($M_{\text{vir},n} = K(n)\sigma_{\text{Re}}^2 R_{\text{Sérsic,circ}}/G$). For LEGA-C only quiescent galaxies are included to create a more direct comparison with the early-type ATLAS^{3D} sample. For LEGA-C we show two flavors of JAM M/L . In red the M/L from the default model with a dark matter component (calculated within R_e) and in black, for direct comparison with ATLAS^{3D}, the model without dark matter.

reaffirming that using R_{circ} instead of R_{sma} serves as a first-order inclination correction on $M_{\text{vir},n}$. Note that the sign of the y-axis is reversed with respect to Figure 6 because we now wish to compare various JAM M/L estimates to a common virial mass estimator ($M_{\text{vir},n}$ from C13). We also note that the scatter (0.12 dex) is larger than in Figure 6 because the Sérsic models have different R_e and L compared to the MGE models that are used for both the JAM and the M_{vir} in Figure 6.

For LEGA-C we have two JAM flavors: our preferred model, which we use in this paper, includes a dark matter component (necessitated by the relatively large extent of the kinematic data, typically $1-3 R_e$), but vH21 also presented self-consistent mass-follows-light models, analogous to the ATLAS^{3D} modeling results used in this section. We calculate JAM M/L for LEGA-C by integrating both the mass and the luminosity within a sphere with radius R_{sma} . The LEGA-C mass-follows-light model M/L shows a 0.09 dex offset with respect to $(M/L)_{\text{vir},n}$, whereas the model with dark matter produces a 0.12 dex offset. This implies that it is not the inclusion of a dark component that elevates the LEGA-C JAM M/L by ≈ 0.1 dex.

The other implication is that the offset in M in the right-hand panel of Figure 3 is due to an offset in M/L . This is not self-evident, as this proportionality rests on the assumption that the sphere with radius R_{sma} includes 50% of the luminosity. This is

not an exact equality, but for the LEGA-C JAM models the difference is small: the fraction of the luminosity within a sphere of radius R_{sma} is, on average, 0.47 ± 0.02 , where the error is the average random error on the individual estimates. This justifies our choice to compare the virial mass estimates with $2 \times$ the dynamical model mass calculated within a sphere with radius R_{sma} (see also Section 4.1).

The offset in M/L implies that, for a given set of observables (q , n , R_e , and σ), M_{JAM} is 0.1 dex larger for LEGA-C than for ATLAS^{3D}. It is not clear whether this offset is physical or the result of an unknown systematic error. There are many differences between higher- and lower-redshift galaxies and between the ATLAS^{3D} and LEGA-C samples. About 50% of the LEGA-C sample are late-type galaxies, with presumably high gas and dark matter fractions relative to the early-type galaxies in ATLAS^{3D}. But also the early-type galaxies in LEGA-C are not equivalent to those in the ATLAS^{3D} sample. The average σ_*^2 is $>2 \times$ higher for LEGA-C, and higher-redshift early-type galaxies are more compact and more rotation dominated. It is therefore not implausible that the dark matter fraction and overall structure is different.

On the pragmatic side, the LEGA-C stellar kinematic data for quiescent (early-type) galaxies typically probe out to $2R_e$ for LEGA-C, which necessitates the inclusion of a dark matter

component, whereas for ATLAS^{3D} this is $1R_e$, for which models with and without dark matter produce very similar total $(M/L)(\lt R_e)$ (C13). It is possible that the LEGA-C $M/L(\lt R_e)$ estimates are biased upward by the statistical weight of kinematic data outside R_e in combination with the low spatial resolution. Kinematic data with higher spatial resolution from, e.g., Extremely Large Telescope is required to resolve this issue. Remaining agnostic about the interpretation of the offset in mass scale between LEGA-C and ATLAS^{3D}, we conclude that we have established a common mass scale for galaxies across 8 Gyr of cosmic time with a small systematic uncertainty of 0.1 dex.

6. Summary and Conclusions

In this paper we provide a new calibration of the mass scale of galaxies at $z=0.6-1$ that is applicable to galaxies of all morphological types. Jeans axisymmetric models for 673 galaxies based on spatially resolved long-slit stellar kinematics from LEGA-C serve as the baseline. Integrated stellar velocity dispersions (the second moment) and Sérsic profiles from HST imaging then allow for virial mass estimates (Equation (7)) with a systematic uncertainty with respect to the locally calibrated mass scale of at most 0.1 dex and with 20% random uncertainty for quiescent galaxies and 40% random uncertainty for star-forming galaxies (Figure 4). The combination of elements to arrive at this level of consistency are as follows:

1. *Nonhomology in radial structure* as parameterized in Equation (4) in order to remove any dependence on galaxy structure (Sérsic index n). Without this correction, and adopting a standard proportionality factor of $K=5$, disk galaxies will have their dynamical masses underestimated by $>50\%$ (Figure 1). We note that the use of $K(n)$ is contingent on the use of the Sérsic profile as a proxy for the light profile, as demonstrated previously by Cappellari et al. (2013).
2. *Nonhomology in 3D galaxy structure* as parameterized in Equation (6) in order to remove any dependence on the projected axis ratio. This accounts for the combined effect of variations in intrinsic, 3D galaxy shape and projection effects. Without such a correction, using the measured, projected velocity second moment (referred to as $\sigma'_{*,\text{int}}$ in this paper), face-on galaxies will have underestimated masses, and edge-on galaxies overestimated masses (Figure 3, left-hand panel).
3. *Half-light radius* as measured along the major axis (R_{sma}), as previously demonstrated by Cappellari et al. (2013).

For convenience we repeat the relevant equations here. The calibrated virial mass estimate is defined as

$$M_{\text{vir}} = K(n)K(q)\frac{\sigma'^2_{*,\text{int}}R_{\text{sma}}}{G}, \quad (9)$$

where

$$K(n) = 8.87 - 0.831n + 0.0241n^2 \text{ (from C13)} \quad (10)$$

and

$$K(q) = (0.87 + 0.38e^{-3.78(1-q)})^2, \quad (11)$$

with the projected axis ratio $q \equiv b/a$.

A comparison with the low-redshift sample of early-type galaxies with integral field spectroscopy data from ATLAS^{3D} shows that the LEGA-C dynamical masses are systematically

higher by 0.1 dex (Section 5.2). It is not clear whether this offset is due to structural differences between the galaxies in the two samples, or due to an unknown systematic error. Nonetheless, we stress that a common mass scale for galaxies across 8 Gyr of cosmic time with a systematic uncertainty of at most 0.1 dex should be considered a success.

Numerous applications, spin-offs and expansions are possible. Practical applications of our calibrated virial mass scale include quick, unbiased dynamical mass estimates for large samples with rudimentary measures of the velocity second moment and size, and the cross-comparison of dynamical masses based on measurements from different instruments.¹⁶ Future work will include a one-to-one comparison between dynamical models based on ionized gas kinematics and stellar kinematics at large lookback time; a comparison with stellar mass estimates, augmented with either direct or inferred gas mass estimates; separating the radial dependence of stellar M/L , gas mass fractions and dark matter fraction (for a smaller subset with highly significant deviations from the mass-follows-light assumption); and a comparison with total masses of galaxies in cosmological hydrodynamical simulations.

Based on observations made with ESO Telescopes at the La Silla Paranal Observatory under program ID 194-A.2005 (The LEGA-C Public Spectroscopy Survey). This project has received funding from the European Research Council (ERC) under the European Union's Horizon 2020 research and innovation program (grant agreement No. 683184).

Appendix

In this Appendix we provide, as a supplement, the dynamical model parameters presented by vH21. The virial mass values were published by van der Wel et al. (2021). In vH21 we already published mass estimates and proxies for dynamical structure (e.g., V/σ), but to facilitate comparisons with other data sets and models we present here all fitted parameters, including those without precise constraints (essentially nuisance parameters required only to marginalize over astrophysically motivated priors). For a full description of the models we refer to vH21, and here we only repeat the important caveats that should be kept in mind when using these data.

In Table 1 we include the M/L estimates for the mass-follows-light model as well as the model that includes a dark component: in addition to the stellar component (as traced by the HST ACS/F814W images) a dark matter component is incorporated. This component serves to account for any M/L gradient, regardless of whether it is actual dark matter, or rather due to gas or stellar M/L variations. While poorly constrained for most individual galaxies (this is reflected in the uncertainties in f_{DM} , which are much larger than the uncertainties in the total M/L) we systematically find for the ensemble that a marginally positive f_{DM} is required to model our kinematic data that probe out to $1-3 R_e$. In short, constraints on f_{DM} reflect a deviation from the mass-follows-light assumption and should not be taken at face value: careful analysis of individual galaxies is required to interpret these quantities.

¹⁶ Subtle differences in integrated σ measurements can be expected when comparing slit- and fiber-based spectra, but at higher redshift the apertures are sufficiently large to render potential aperture corrections small compared to the uncertainties on the mass estimates.

Table 1
LEGA-C JAM Parameters (Models with Dark Component)




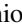







| ID1 | ID2 | $\log(L)$ $L_{\odot,g}$ | $\log(M/L)$ (no DM) $M_{\odot}/L_{\odot,g}$ | $\log(M/L)$ (with DM) $M_{\odot}/L_{\odot,g}$ | f_{DM} | β_z | i deg. |
|-----|-------|----------------------------|--|--|------------------------|-------------------------|-------------|
| 5 | 4792 | 10.87 | $0.05^{+0.05}_{-0.03}$ | $0.34^{+0.27}_{-0.24}$ | $0.62^{+0.38}_{-0.42}$ | $0.03^{+0.33}_{-0.35}$ | 28 ± 4 |
| 26 | 10462 | 10.73 | $-0.24^{+0.06}_{-0.05}$ | $0.15^{+0.46}_{-0.36}$ | $0.71^{+0.29}_{-0.58}$ | $0.02^{+0.32}_{-0.36}$ | 44 ± 5 |
| 27 | 10902 | 11.35 | $0.09^{+0.05}_{-0.03}$ | $0.43^{+0.48}_{-0.42}$ | $0.62^{+0.38}_{-0.52}$ | $-0.03^{+0.34}_{-0.33}$ | 31 ± 4 |
| 38 | 14375 | 11.25 | $0.14^{+0.02}_{-0.02}$ | $0.17^{+0.07}_{-0.08}$ | $0.10^{+0.76}_{-0.09}$ | $-0.07^{+0.34}_{-0.29}$ | 74 ± 5 |
| 39 | 14729 | 11.37 | $0.47^{+0.05}_{-0.04}$ | $0.42^{+0.32}_{-0.40}$ | $0.00^{+1.00}_{-0.00}$ | $0.19^{+0.23}_{-0.41}$ | 67 ± 6 |
| : | : | : | : | : | : | : | : |

Note. JAM model parameters described by [vH21](#). Col. (1): LEGA-C ID (DR3). Col. (2): UltraVISTA ID (Muzzin et al. 2013b). Col. (3): g -band mass-to-light from the mass-follows-light model. Col. (4): total g -band mass-to-light ratio from the light plus dark matter (DM) model. Col. (5): dark matter fraction. Col. (6): inclination, Col. (7): vertical anisotropy $\beta_z \equiv 1 - \langle v_z^2 \rangle / \langle v_R^2 \rangle$. All quantities are calculated within spherical apertures with radius $R_{\text{Sersic, sma}}$. Values and uncertainties are based on 16th, 50th, 84th percentiles of posterior parameter distributions. The machine-readable table has 861 entries and is matched to the catalog published in [vH21](#).

(This table is available in its entirety in machine-readable form.)

Inclinations are almost always unconstrained by the kinematic data due to the relatively poor spatial resolution and large width of the slit. The estimates in the table are therefore the result of the marginalization over the prior, which is set by the projected shape of the HST light profile (see [vH21](#) for further details).

ORCID iDs

Arjen van der Wel  <https://orcid.org/0000-0002-5027-0135>
 Rachel Bezanson  <https://orcid.org/0000-0001-5063-8254>
 Marijn Franx  <https://orcid.org/0000-0002-8871-3026>
 Francesco D'Eugenio  <https://orcid.org/0000-0003-2388-8172>
 Caroline Straatman  <https://orcid.org/0000-0001-5937-4590>
 Eric F. Bell  <https://orcid.org/0000-0002-5564-9873>
 Adam Muzzin  <https://orcid.org/0000-0002-9330-9108>
 David Sobral  <https://orcid.org/0000-0001-8823-4845>
 Michael V. Maseda  <https://orcid.org/0000-0003-0695-4414>
 Anna de Graaff  <https://orcid.org/0000-0002-2380-9801>
 Bradford P. Holden  <https://orcid.org/0000-0002-6153-3076>

References

- Belli, S., Newman, A. B., & Ellis, R. S. 2014, *ApJ*, 783, 117
 Belli, S., Newman, A. B., & Ellis, R. S. 2017, *ApJ*, 834, 18
 Bender, R., Burstein, D., & Faber, S. M. 1992, *ApJ*, 399, 462
 Bezanson, R., van der Wel, A., Pacifici, C., et al. 2018b, *ApJ*, 858, 60
 Bezanson, R., van der Wel, A., Straatman, C., et al. 2018a, *ApJL*, 868, L36
 Bezanson, R., van Dokkum, P. G., Tal, T., et al. 2009, *ApJ*, 697, 1290
 Brinchmann, J., Charlot, S., White, S. D. M., et al. 2004, *MNRAS*, 351, 1151
 Bundy, K., Bershady, M. A., Law, D. R., et al. 2015, *ApJ*, 798, 7
 Cappellari, M. 2002, *MNRAS*, 333, 400
 Cappellari, M. 2008, *MNRAS*, 390, 71
 Cappellari, M. 2017, *MNRAS*, 466, 798
 Cappellari, M., Bacon, R., Bureau, M., et al. 2006, *MNRAS*, 366, 1126
 Cappellari, M., & Emsellem, E. 2004, *PASP*, 116, 138
 Cappellari, M., Scott, N., Alatalo, K., et al. 2013, *MNRAS*, 432, 1709
 Chang, Y.-Y., van der Wel, A., Rix, H.-W., et al. 2013, *ApJ*, 773, 149
 Ciotti, L. 1991, *A&A*, 249, 99
 Dressler, A., Lynden-Bell, D., Burstein, D., et al. 1987, *ApJ*, 313, 42
 Emsellem, E., Cappellari, M., Krajnović, D., et al. 2007, *MNRAS*, 379, 401
 Emsellem, E., Cappellari, M., Krajnović, D., et al. 2011, *MNRAS*, 414, 888
 Gallazzi, A., Bell, E. F., Zibetti, S., Brinchmann, J., & Kelson, D. D. 2014, *ApJ*, 788, 72
 Gallazzi, A., Charlot, S., Brinchmann, J., White, S. D. M., & Tremonti, C. A. 2005, *MNRAS*, 362, 41
 Guérou, A., Krajnović, D., Epinat, B., et al. 2017, *A&A*, 608, A5
 Hopkins, P. F., Bundy, K., Hernquist, L., Wuyts, S., & Cox, T. J. 2010, *MNRAS*, 401, 1099
 Jorgensen, I., Franx, M., & Kjaergaard, P. 1996, *MNRAS*, 280, 167
 Kelvin, L. S., Driver, S. P., Robotham, A. S. G., et al. 2012, *MNRAS*, 421, 1007
 Koekemoer, A. M., Aussel, H., Calzetti, D., et al. 2007, *ApJS*, 172, 196
 Krajnović, D., Alatalo, K., Blitz, L., et al. 2013, *MNRAS*, 432, 1768
 Li, H., Mao, S., Cappellari, M., et al. 2018, *MNRAS*, 476, 1765
 Mosleh, M., Tacchella, S., Renzini, A., et al. 2017, *ApJ*, 837, 2
 Muzzin, A., Marchesini, D., Stefanon, M., et al. 2013a, *ApJS*, 206, 8
 Muzzin, A., Marchesini, D., Stefanon, M., et al. 2013b, *ApJ*, 777, 18
 Naab, T., Johansson, P. H., & Ostriker, J. P. 2009, *ApJL*, 699, L178
 Newman, A. B., Belli, S., Ellis, R. S., & Patel, S. G. 2018, *ApJ*, 862, 126
 Noeske, K. G., Weiner, B. J., Faber, S. M., et al. 2007, *ApJL*, 660, L43
 Peng, C. Y., Ho, L. C., Impey, C. D., & Rix, H.-W. 2010, *AJ*, 139, 2097
 Sánchez, S. F., Kennicutt, R. C., Gil de Paz, A., et al. 2012, *A&A*, 538, A8
 Scott, N., van de Sande, J., Croom, S. M., et al. 2018, *MNRAS*, 481, 2299
 Shen, S., Mo, H. J., White, S. D. M., et al. 2003, *MNRAS*, 343, 978
 Shetty, S., & Cappellari, M. 2015, *MNRAS*, 454, 1332
 Straatman, C. M. S., van der Wel, A., Bezanson, R., et al. 2018, *ApJS*, 239, 27
 Suess, K. A., Kriek, M., Price, S. H., & Barro, G. 2019, *ApJ*, 877, 103
 Szomoru, D., Franx, M., van Dokkum, P. G., et al. 2013, *ApJ*, 763, 73
 Taylor, E. N., Franx, M., Brinchmann, J., van der Wel, A., & van Dokkum, P. G. 2010, *ApJ*, 722, 1
 Toft, S., Gallazzi, A., Zirm, A., et al. 2012, *ApJ*, 754, 3
 van de Sande, J., Kriek, M., Franx, M., et al. 2013, *ApJ*, 771, 85
 van de Ven, G., & van der Wel, A. 2021, *ApJ*, 914, 45
 van der Wel, A., Bell, E. F., Häussler, B., et al. 2012, *ApJS*, 203, 24
 van der Wel, A., Bezanson, R., D'Eugenio, F., et al. 2021, *ApJS*, 256, 44
 van der Wel, A., Chang, Y.-Y., Bell, E. F., et al. 2014b, *ApJL*, 792, L6
 van der Wel, A., Franx, M., van Dokkum, P. G., et al. 2014a, *ApJ*, 788, 28
 van der Wel, A., Franx, M., Wuyts, S., et al. 2006, *ApJ*, 652, 97
 van der Wel, A., Noeske, K., Bezanson, R., et al. 2016, *ApJS*, 223, 29
 van der Wel, A., & van der Marel, R. P. 2008, *ApJ*, 684, 260
 van Dokkum, P. G., & van der Marel, R. P. 2007, *ApJ*, 655, 30
 van Houdt, J., van der Wel, A., Bezanson, R., et al. 2021, *ApJ*, 923, 11
 Wu, P.-F., van der Wel, A., Bezanson, R., et al. 2018, *ApJ*, 868, 37